



## Article

# Near-Perfect Infrared Transmission Based on Metallic Hole and Disk Coupling Array for Mid-Infrared Refractive Index Sensing

Lingyi Xu <sup>1</sup> , Jianjun Lai <sup>1,\*</sup> , Qinghua Meng <sup>2</sup>, Changhong Chen <sup>1</sup> and Yihua Gao <sup>3</sup>

<sup>1</sup> Wuhan National Laboratory for Optoelectronics, Huazhong University of Science and Technology, Wuhan 430074, China; xulingyi@hust.edu.cn (L.X.); ch\_chen@mail.hust.edu.cn (C.C.)

<sup>2</sup> School of Physics and Electronics, Nanning Normal University, Nanning 530299, China; mqhgx@163.com

<sup>3</sup> School of Physics, Huazhong University of Science and Technology, Wuhan 430074, China; gaoyihua@hust.edu.cn

\* Correspondence: jjlai@hust.edu.cn

**Abstract:** Nanostructured color filters, particularly those generated by the extraordinary optical transmission (EOT) resonance of metal–dielectric nanostructures, have been intensively studied over the past few decades. In this work, we propose a hybrid array composed of a hole array and a disk array with the same working period within the 3–14  $\mu\text{m}$  mid-infrared band. Through numerical simulations, near-perfect transmission (more than 99%) and a narrower linewidth at some resonance wavelengths were achieved, which is vital for highly sensitive sensing applications. This superior performance is attributed to the surface plasmon coupling resonance between the hole and disk arrays. A high tunability of the near-perfect transmission peak with varying structural parameters, characteristics of sensitivity to the background refractive index, and angle independence were observed. We expect that this metallic hole and disk coupling array is promising for use in various applications, such as in plasmon biosensors for the high-sensitivity detection of biochemical substances.

**Keywords:** microhole array; microdisk array; extraordinary optical transmission; coupling resonance; plasmon resonance sensor; mid-infrared band; refractive index sensor



**Citation:** Xu, L.; Lai, J.; Meng, Q.; Chen, C.; Gao, Y. Near-Perfect Infrared Transmission Based on Metallic Hole and Disk Coupling Array for Mid-Infrared Refractive Index Sensing. *Chemosensors* **2024**, *12*, 3. <https://doi.org/10.3390/chemosensors12010003>

Received: 7 November 2023

Revised: 22 December 2023

Accepted: 23 December 2023

Published: 26 December 2023



**Copyright:** © 2023 by the authors. Licensee MDPI, Basel, Switzerland. This article is an open access article distributed under the terms and conditions of the Creative Commons Attribution (CC BY) license (<https://creativecommons.org/licenses/by/4.0/>).

## 1. Introduction

Metallic plasmonic sensors are widely used in biosensing and chemical-sensing applications. Nanostructured metallic plasmon sensors have advantages, including easier coupling access for exciting the resonance, owing to the nanostructure's extra momentum for matching, as well as the high sensitivity of the local electromagnetic field to changes in the surrounding dielectric environment. These benefits have aroused extensive interest in the development of various sensor platforms that support surface lattice resonance [1–4], Fano resonance [5–7], surface-enhanced Raman scattering (SERS) [8,9], extraordinary optical transmission (EOT) of metallic nanohole arrays [9–13], or plasmon-enhanced optical fiber sensing [14–16] for use in applications such as ultrasensitive biomolecular detection [17], photocatalysis [18–21], temperature/pressure monitoring [22], metal-enhanced fluorescence detection [23], and microfluid point-of-care diagnostics [24]. To date, nanostructured plasmon sensors have been widely investigated due to their wide electromagnetic radiation ranging from the UV to the THz band, but their dominant band is the visible to near-infrared band, where the excitation of surface plasmon polaritons (SPPs) based on commonly used noble metals (Ag, Au, and Cu) is easily achieved [19,25,26]. Mid-infrared plasmon sensors have also attracted attention, and some progress has been made in this area [27–30]. This is attributed to the fact that in the mid-infrared band, the good accuracy and sensitivity of surface plasmon resonance (SPR) sensors when utilized with larger samples such as living cells, and the good immunity of biological samples to photodamage or phototoxicity caused by the light source, are easily preserved [31].

Among the aforementioned plasmon sensors, EOT-based sensors have many advantages over conventional SPR techniques. For example, because an EOT-based optical signal has no optical noise originating from reflected light, a high signal-to-noise ratio can be obtained [32]. Conceptually, EOT refers to electromagnetic resonances that pass through nanohole arrays in metal films, providing a larger transmission of electromagnetic fields than that expected from the small nanohole size. Since its discovery in 1998, EOT has led to the discovery of new ways of enhancing optical transmission as well as decreasing linewidth (thus leading to a high-quality factor  $Q$ ) [33], and it has been applied in sensing, filters, and optical trapping [34]. Different approaches to develop hybrid nanostructures have been proposed to enhance the optical transmission and/or  $Q$  to surpass the performance of a simple nanohole array [35–37]. A typical approach is to introduce nanomaterials into the nanohole array and create a coupling in the surface plasmon mode between the nanoholes and nanomaterials in the compound structure [1,38]. For example, a nanohole array with a nanorod in its center achieved a maximum transmission of 56%, compared with a transmission of 37% of a none-in-hole nanohole array gold film [38]. Another approach is to employ coupling between plasmon and optical cavity modes. For example, a three-zone structure composed of a top metal grating,  $\text{SiO}_2$  spacer, metal film, and silicon substrate was shown to have a transmission of 84% in the near-infrared regime, and was robust under oblique incidence with TM polarization [39]. Other schemes, such as cavity-coupled metal–insulator–metal (MIM) nanohole array structures on quartz substrates, were observed to exhibit a coupling effect between the SPP mode on the metal–insulator interface and the gap SPP in the gap cavity in the near-infrared regime, leading to a linewidth reduction and  $Q$  improvement [40]. Although great efforts have been made to pursue the goal of perfect transmission and an ultrahigh  $Q$  for sensing applications, developing new, advanced nanostructures and the optimization of relevant parameters to maximally strengthen the coupling resonance are critical and still present a challenge.

In this study, a hybrid structure with Al holes and disks on a silicon substrate is proposed. Compared to existing hybrid structures that directly construct a disk or disks in/on the hole, the proposed structures are constructed with a disk on the surface of the metal film near the hole, only a short distance away. Based on numerical investigation using FDTD simulation, under the condition of structural matching, specific wavelengths in the mid-infrared band were found to transmit at an extremely high transmission rate (99.1%) and have a smaller full width at half maximum (FWHM) compared with those of a pure microhole array. In addition, to study the selectivity of the structure in regard to light waves, the influence of modifying different parameters on the transmission performance was analyzed in detail. These results show that the Al microhole–microdisk hybrid array has high sensitivity and a large figure of merit (FOM) as a refractive index sensor, meaning it has potential applications in molecular or living cell detection.

## 2. Results and Discussions

### 2.1. Principle of Coupling EOT

When the periods of the metal hole and disk arrays are much smaller than the wavelength, EOT can be formed in the metal thin-film structure. This phenomenon is mainly caused by the interaction between the light wave and free electron oscillation at the surface of the metal hole array, or in other words, the interaction between surface plasmon polaritons (SPPs) and local surface plasmon resonance (LSPR) on the surface of the metal disks. SPPs are evanescent waves propagating along a metal surface that are generated by the interaction between electrons and photons freely oscillating on the metal surface. They propagate along the metal surface and can be converted into a transmitted field at the hole, which is the dominant factor in EOT. As shown in Figure 1a, the incident light  $E_0$  excited the evanescent wave electric field  $E_{\text{surf}}$  on the metal surface, was transmitted to the hole, and formed a new electric field  $E_{\text{st}}$ . The wavelength of the EOT is affected by the period of the hole. LSPR is the plasmon resonance behavior of metal microdisk surfaces under the illumination of light waves. In the abnormal optical transmission of porous metal films,  $E_t$

is mainly affected when light passes through the holes, as shown in Figure 1a. In general, the excitation of SPPs mainly depends on the distance between metal holes; therefore, metal holes with different periods can excite EOTs of different wavelengths. The wavelength corresponding to the excited surface plasma wave satisfies the following equation:

$$k_{SPP} = k_0 \sqrt{\frac{\epsilon_m \epsilon_d}{\epsilon_m + \epsilon_d}}, \quad (1)$$

$$k_{spp} = k_0 \cdot \sin \theta + \sqrt{(i^2 + j^2)} \cdot \frac{2\pi}{P} \quad (2)$$

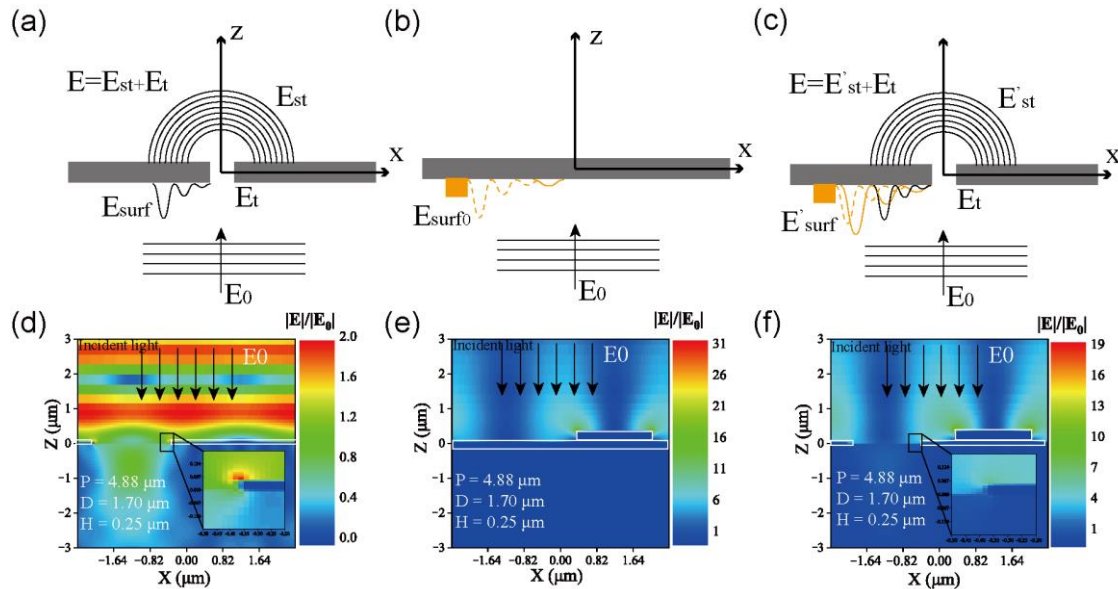


**Figure 1.** Schematic view of resonance and coupling effect when the incident field impinges on a metal film with hole and/or disk. (a) EOT of metal hole. (b) Excitation of LSPR by metal disk. (c) Enhanced EOT due to the coupling of SPP from metal film with hole array and LSPR from metal disk. (d–f) Cross-sectional distribution of electric field intensities at incident light wavelength of 3.5  $\mu\text{m}$  for hole, disk, and hybrid structures, respectively; when both the hole and disk arrays have periods of 4.88  $\mu\text{m}$ , both the hole and disk have diameters of 1.70  $\mu\text{m}$ , and the thicknesses of the metal film and disk are the same at 0.25  $\mu\text{m}$ .

Here,  $i$  and  $j$  are integers,  $\epsilon_m$  is the real part of the dielectric constant of the metal,  $\epsilon_d$  is that of the dielectric, and  $P$  is the period of the square lattice. Using Equation (1), one can calculate the wave vector of the surface plasmon excitations at the interface between metal and air, as well as that between metal and silicon. Using Equation (2), one can calculate the order of SPPs for the hole structure under different periodic conditions. Under a normal incidence where  $\theta = 0$ , the excitation wavelengths of the surface plasmon are given by

$$\lambda_{spp}(i, j) = \frac{P}{\sqrt{i^2 + j^2}} \sqrt{\frac{\epsilon_m \epsilon_d}{\epsilon_m + \epsilon_d}} \quad (3)$$

Based on Equation (3), the resonant positions are distinguishable for the metal/air and metal/substrate interfaces with different mode orders.

When there is only a protrusion structure, as shown in Figure 1b, surface plasma waves can only be excited between the protrusion disk structure and air, and the metal film is thick enough to result in very low transmission. Most incident light waves are reflected, and only the wavelength that resonates with the metal–disk structure can generate surface plasma waves. Therefore, no EOTs can be generated, and only a small amount of the surface plasma wave is absorbed.

If the two structures are combined, as shown in Figure 1c, the evanescent wave formed by the metal hole and metal disk structures is coupled, and a new electric field is formed through the metal hole. At this time, only the wavelength that meets the requirements of the simultaneous resonance of the metal hole and metal disk structures can be enhanced, and thus, the transmitted electric field is enhanced.

The coupling enhancement of the EOT of the hybrid structure is demonstrated by the electric field distribution shown in Figure 1d–f, where a set of typical structural parameters has been chosen as an example. We can see that the output field strength of the simple hole array is approximately 1.2, and that of the mixed structure is approximately 2.9 (taking the center of the hole and the wavelength of the incident light to be  $3.5\ \mu\text{m}$ ), which is increased 2.4-fold.

## 2.2. Structures and Simulation

A three-dimensional finite-difference time-domain method (FDTD Solutions, Lumerical Solutions Inc, Vancouver, Canada.) was used to simulate the structures. A thin metal film with an array of circular microholes was placed on the silicon substrate surface and a periodic metal circular microdisk was placed in the blank area. Three configurations were employed for the simulation: (1) a pure metal microhole array, (2) a pure metal microdisk array, and (3) a coupled array structure of staggered microholes and microdisks, as shown in Figure 2a. The influences of the period  $P$ , microhole radius  $r$ , and height  $h$  of the microdisk arrays on these structures are analyzed in the following sections. The definitions of these parameters are shown in Figure 2b.

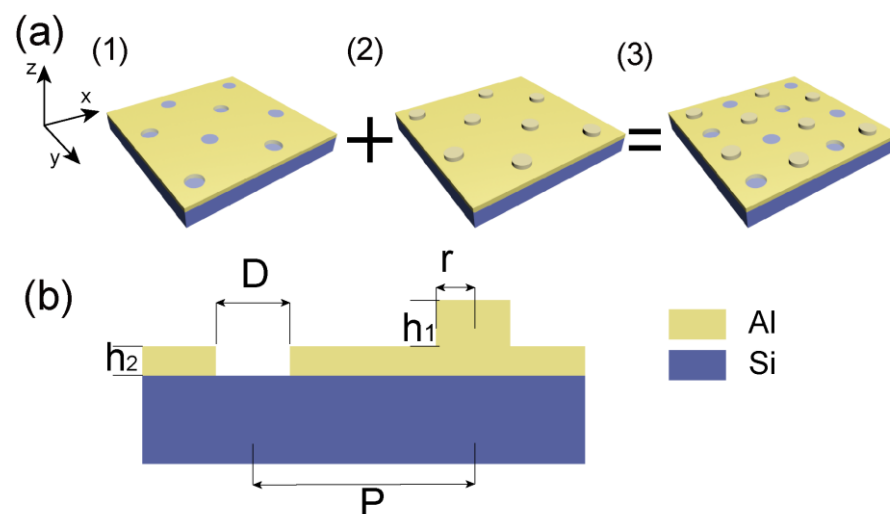


**Figure 2.** (a) (1) shows a porous metal surface plasmon structure, while (2) shows a metal thin-film structure with Al disk protrusions. These structures are combined to form a near-perfect infrared transmission and angle-insensitive filter for a metallic hole and disk coupling array in (3). (b) Sectional schematic diagram and structural parameters of the device.

In the simulation process, the dielectric constants of the metal film and metal microdisk were obtained from the FDTD database. The incident light was selected as a plane wave propagating in the negative  $z$ -direction with electric field polarization in the  $x$ -direction. The wavelength range of the incident light covered a broad infrared band ( $3\text{--}14\ \mu\text{m}$ ), which was used to calculate the transmission spectra. Periodic boundary conditions were set in both the  $x$ - and  $y$ -directions, whereas a perfectly matched layer boundary condition was used on the  $z$ -axis.

A schematic diagram of the structures and the simulation results is shown in Figure 3. The structure with only metal disks on the metal thin film is shown in Figure 3a, and its reflection spectrum is shown in Figure 3b, indicating two absorption peaks at  $3.5\ \mu\text{m}$  and  $5\ \mu\text{m}$  owing to the excitation of the surface plasmon polariton when light irradiates the

metal structure. Due to the fact that the thickness of the metal film is greater than its skin depth, there is no light transmission through the metal film. From Figure 3c, we can see that the magnetic field of 3.5  $\mu\text{m}$  is mainly concentrated near the metal disks, and it can be assumed that the surface plasmon resonance is excited in this structure. According to Equation (3), when only a porous metal film structure exists, as shown in Figure 3d, the surface plasmons can be excited at different wavelengths, as shown in Figure 3e. It was found that there is a (2,2) mode-order plasmon resonance at 3.5  $\mu\text{m}$ , and the quality factor of this resonance mode is about  $Q = 14.75$  ( $Q = \lambda_R/\text{FWHM}$ ), where  $\lambda_R$  is the resonance wavelength. However, no surface plasmons are excited at 5  $\mu\text{m}$ . As shown in Figure 3f, the magnetic field distribution of the (2,2) mode-order infrared radiation shows a partial transmission. When the two structures are combined, as shown in Figure 3g,h, the surface plasmon mode excited by the pore structure exhibits resonance at 3.5  $\mu\text{m}$ , but does not exhibit a resonance phenomenon at 5  $\mu\text{m}$ . It can be concluded that the surface plasmons excited by the two structures together at 3.5  $\mu\text{m}$  are coupled to enhance the abnormal transmission at this wavelength. From Figure 3h, the quality factor of the coupled mode can be calculated to be about 28.1, and the coupling of the two structures increases the quality factor by 100%. From Figure 3i, we can see that the amplitude of the magnetic field of the (2,2) mode-order infrared wavelength is enhanced by several orders of magnitude compared to that of the pure microhole array shown in Figure 3f.

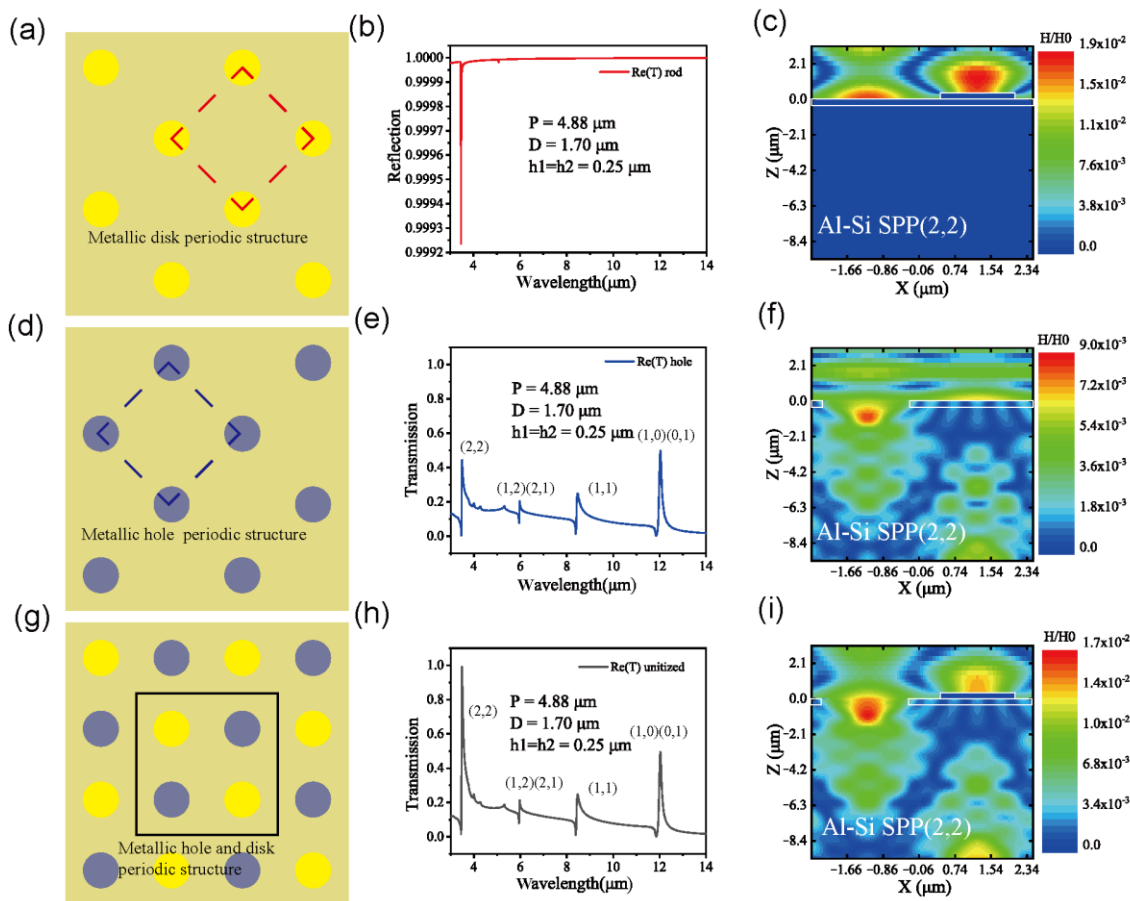


**Figure 3.** (a) Schematic view of metal perforated film with disk array. (b) The infrared reflectance spectrum of metal disk array structure. (c) The magnetic field strength of metal disk structure. (d) Schematic view of metal film with hole array. (e) The infrared transmission of metal hole array structure. (f) The magnetic field strength of metal hole structure. (g) Schematic view of metal hole and metal disk coupling structure. (h) Simulated infrared transmission spectrum of coupled metal hole and disk structure. (i) The magnetic field strength of metal hole and disk structure when coupling.

To determine the effect of the surface metal disk array on this abnormal transmission enhancement, the structural parameters of the metal disk array were adjusted. The height of the metal disk was modified from 50 nm to 260 nm, and the change in its transmission spectrum is shown in Figure 4a. It can be seen from the figure that there is a small change in the transmission at different heights; however, the transmission is maximal at the same height (when the height is 260 nm, the transmission is 98.4%, which is less than that at a height of 250 nm). In addition, the radius of the metal disk was adjusted and the transmission was changed, as shown in Figure 4b. It can be observed that transmission is optimal when the metal disk structure is consistent with the metal pore structure.

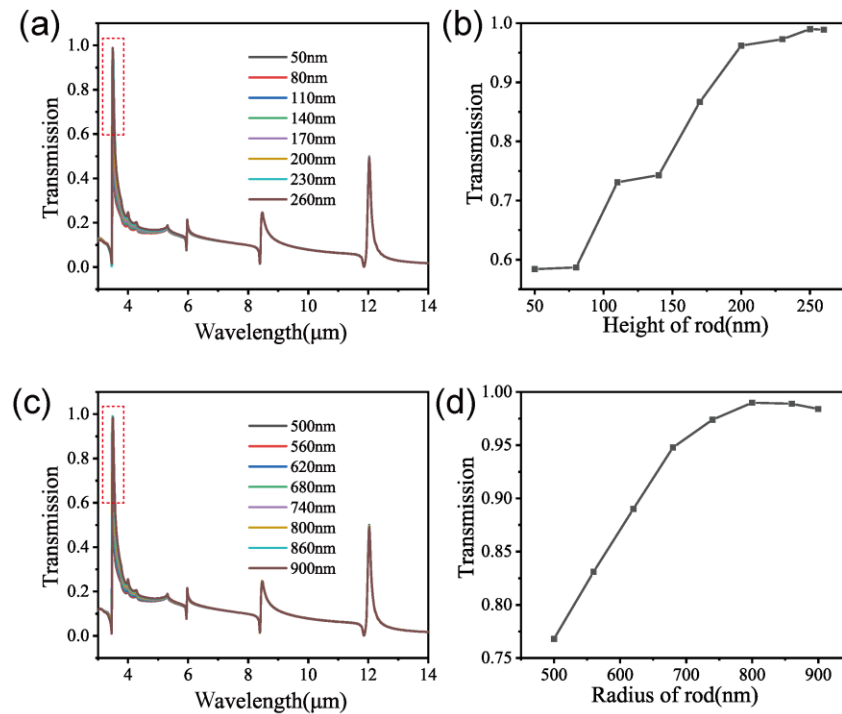


**Figure 4.** (a,b) Transmission spectra of the coupled array as a function of surface height of disk microstructure when fixing metal hole films so that the thickness of the metal hole film is 250 nm, and the period of the hole and disk is 4.88  $\mu\text{m}$ . (c,d) Transmission spectra of the coupled array as a function of radius of disk microstructure. Additionally, the thickness of the metal hole film and the height of the disk are both 250 nm, and the period of the hole and disk remains unchanged.

Next, we changed the shape and number of metal disks while keeping the microhole array unchanged. We simulated the transmission spectra of coupled structures with square metal disks, triangular metal disks, and single cylindrical metal disks, and obtained the simulated results shown in Figure 5. Among the disks of different shapes, the side length of the square disk was 850 nm with a height of 250 nm, whereas the triangular disk was an equilateral triangle with a side length of 850 nm and a height of 250 nm. From Figure 5a,b, it can be observed that the positions of the transmission peaks are not influenced by the shape of the microdisk, but the transmission at each peak changes more or less, indicating the period dependency of the SPP wavelength and the microdisk dependency of the transmission for the proposed structures. Figure 5c shows the transmission spectrum of the structure with only one cylinder bulge in one cycle. It was found that the transmission decreases significantly at 3.5  $\mu\text{m}$  compared with that of the two-cylinder structures, demonstrating the enhancement function of the microdisk again.

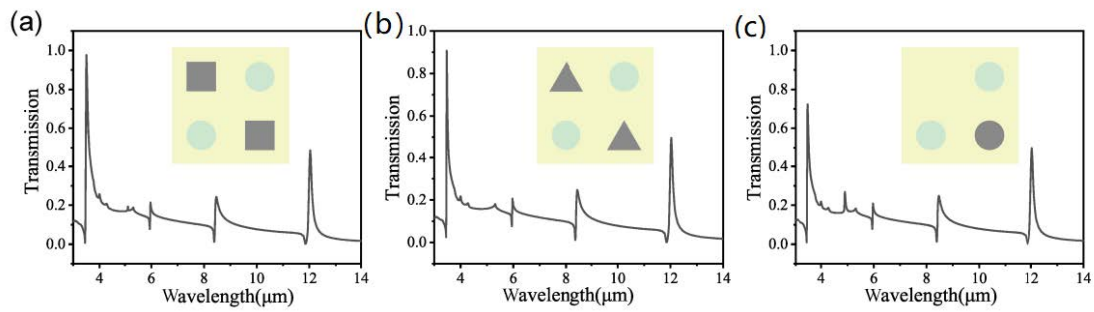


**Figure 5.** (a) Transmission spectrum of the compound structure as circular microdisks are replaced by square microdisks. (b) Transmission spectrum of the compound structure as the circular microdisks are replaced by triangular microdisks. (c) Transmission spectrum of compound structure with only one microdisk in one cell of the array.

To study the practical applicability of the device in real scenarios, we evaluated the effect of variations in the angle and polarization state of the incident light on the transmission performance. As shown in Figure 6a, the transmission peak is insensitive to the incidence angle; however, the intensity of the transmission peak gradually decreases with an increasing angle of incidence. In contrast, a device without a metal disk was simulated under the same conditions to examine the angular response of transmission. The results are shown in Figure 6b. When a metal disk was present, the transmission decreased with an increase in the angle, indicating that the metal disk improved the filter’s sensitivity to the incident light angle. It can be observed that when the incidence angle increases to 30°, there is still 50% transmission in Figure 6a and only 28% transmission in Figure 6b, which makes detection more difficult. As the device satisfied the conditions of rotational symmetry, it was insensitive to the polarization of incident light, as shown in Figure 6c.

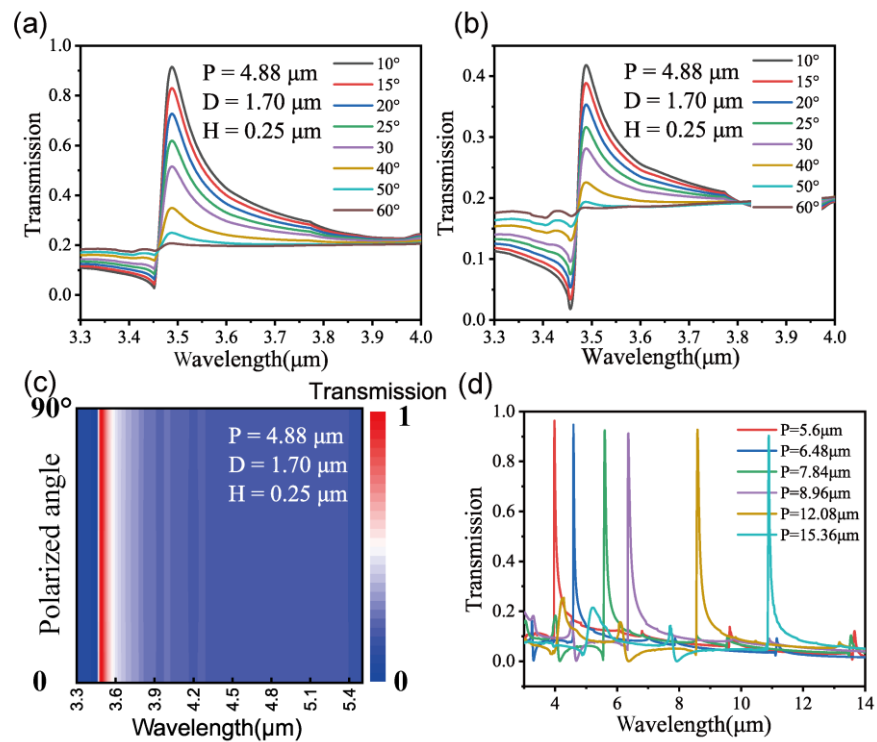


**Figure 6.** Relation between incident light angle and transmission when the device has a metal disk (a) and does not have a metal disk (b). (c) Relation between polarization state and transmission of incident light. (d) The device’s transmission under different periods.

By modifying the structural parameters of the coupled hole–disk array, very high transmission under different wavelength conditions can be obtained; thus, near-perfect transmission can be achieved in a broadband range covering the medium- and long-wave infrared regions, as shown in Figure 6d. Table 1 lists the device parameters corresponding to the transmission peaks shown in Figure 6d.

**Table 1.** Transmission intensities and linewidths of coupled resonances at optimum structure parameters according to Figure 6d.

Resonance wavelength ( $\mu\text{m}$ )	3.97	4.58	5.60	6.36	8.59	10.89
Parameters ( $\mu\text{m}$ ) P/D/(h1, h2)	5.6/1.84/0.3	6.48/1.92/0.35	7.84/2.16/0.45	8.96/2.7/0.6	12.08/3.2/0.8	15.3/6.4/1.0
FWHM (nm)	78	41	88	76	65	52
$T_{\text{max}}$	0.96	0.93	0.91	0.9	0.92	0.9

### 2.3. Analysis of Refractive Index Sensing

Compared to the refractive index sensors extensively investigated in the visible and near-infrared wavebands, their counterparts in the mid-infrared band have unique advantages, including the accuracy and sensitivity of SPR sensors when used on larger samples, such as living cells, as well as biological samples receiving low photodamage or phototoxicity levels from the mid-infrared light source [27]. Therefore, interest in studying and developing SPR devices in the mid-IR range has been maintained through various schemes, such as the study of fiber-optic-based structures [38], graphene nanoribbon structures [28], and black phosphorous-based nanostructures [41]. For a refractive index sensor, the sensitivity (S) and figure of merit (FOM) are important parameters for performance evaluation. S and FOM can be expressed as  $S = \Delta\lambda/\Delta n$  and  $\text{FOM} = S/\text{FWHM}$ , respectively. Owing to the narrow linewidth, near-perfect transmission, and intrinsic sensitivity to the surrounding circumstances, the coupling-array-based sensor proposed here is expected to exhibit a highly sensitive performance in the mid-infrared band.

To examine the sensing performance of the proposed coupled sensor, the dependence of the transmission spectrum on different surrounding or background refractive indices was calculated while the other parameters were fixed. The background refractive index parameters can be set in the FDTD according to the different background refractive indices from 1.1 to 1.38, which can be used for any gas or liquid. As shown in Figure 7a, the resonant transmission peak at 3.5  $\mu\text{m}$  has a remarkable red shift with an increase in the background refractive index, whereas the other resonant peaks are basically unchanged. In this study, the S parameter was 3.521  $\mu\text{m}/\text{RIU}$  and the FOM was approximately 20, as shown in Figure 7b. Table 2 shows a comparison of the sensitivity (S) and figure of merit (FOM) of different structures proposed in previous studies. It can be clearly seen that the proposed structure exhibits a better sensing performance.

**Table 2.** Comparison of performances of various infrared plasmon resonance sensors proposed in previous publications with that of this work.

Principle	Wavelength ( $\mu\text{m}$ )	Sensitivity (Max) ( $\mu\text{m}/\text{RIU}$ )	FOM (Max)	References
Plasmonic perfect absorber (PA) based on graphene metamaterials	22.5	5.6	10.8	[41]
Photonic crystal fiber	3.4	9	/	[27]
EOT from two metal nano-slit arrays	1.8–1.96	1.435	80	[42]
MIM plasmon absorber	2.9	2.44	84	[43]
Coupled Al hole–disk array	3.5	3.521	20	This work

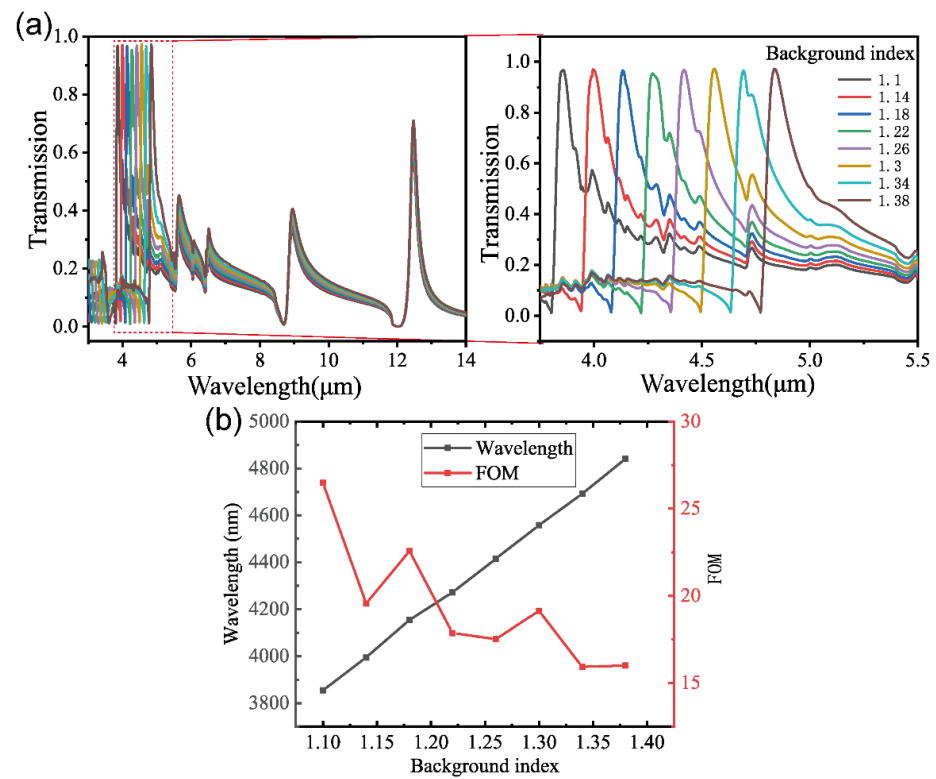


**Figure 7.** (a) Change in transmission of the device under different background index conditions. (b) The resonance wavelength variation for the state of the background refractive index of the object ranging from 1 to 1.38 in 0.04 intervals.

#### 2.4. Fabrication and Testing

A plasmonic coupled structure with a microhole and microdisk array was fabricated on the surface of a high-resistivity monocrystalline silicon substrate. Firstly, a stepper lithography machine (500 nm precision stepper lithography machine, NSR-220519C, Nikon (Nikon Corporation, Tokyo, Japan)) was used to create a photolithographic pattern of metal holes on the surface of the silicon wafer, and an 80 nm thick Al film was coated on the surface by means of electron beam evaporation. After peeling, an 80 nm thick Al film with a hole array was obtained. Then, a 200 nm thick Al disk array was fabricated on the surface of the Al film using a lift-off process including photolithography and electron beam evaporation. Scanning electron microscopy (SEM) (FEI Company, Hillsboro, OR, USA) was used to measure the geometrical parameters of the pure microhole array structure and the hybrid structure with hole and disk arrays. SEM images of the pure microhole array are shown in Figure 8a, and an enlarged image is shown in Figure 8b after the microhole arrays were fabricated. It can be seen that the diameter and period of the microhole array are 2.2 μm and 2.6 μm, respectively. The Al film thickness was 82 nm, as measured using a step meter (Bruker DektakXT, Bruker Corporation, Billerica, MA, USA). After the metal microdisk structure was made, SEM of the compound structure was carried out, as shown in Figure 8c,d, where the diameter and period of the disk were 1.64 μm and 2.6 μm, respectively, and the height of the disk was 194 nm. Obviously, the fabricated microhole and microdisk are not perfectly shaped circles and also are not the right diameters based on the designed values. In the SEM pictures shown in Figure 8, the white edges on the disks and holes indicate that the fabricated cylindrical structures are surrounded by large slopes, which deviate from the ideal vertical cylindrical structures our simulation required, thus affecting the transmission spectra.

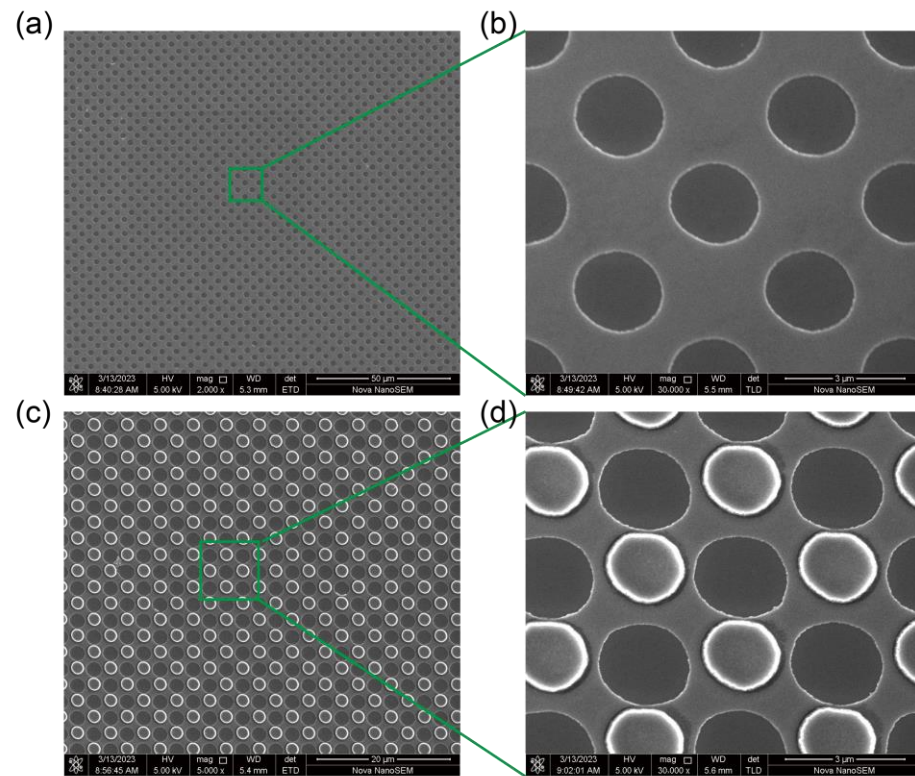


**Figure 8.** (a,b) SEM image of metal hole array. (c,d) SEM image of hybrid hole–disk array.

Next, a Nicolet iN10 microscopic infrared spectrometer (Thermo Fisher Scientific, Waltham, MA, USA) was used to measure the transmission spectra of the fabricated structures with and without the microdisk arrays. The measured results for different array periods are shown in Figure 9, where the transmission curves of the hybrid structure, represented in black, are compared with that of the pure metal hole structure, represented in red. It can be seen that there is a significantly enhanced transmission for compound structures from 4 to 6  $\mu\text{m}$  in the mid-infrared band, with peaks at 4.6, 5.1, and 5.5  $\mu\text{m}$  corresponding to periods of 5.2, 5.6, and 5.8  $\mu\text{m}$ , respectively, as compared to that of structures without microdisks. As shown in Figure 9a, the maximum enhancement effect is only carried out at the mid-wave infrared wavelength of 4.7  $\mu\text{m}$ , while the enhancement cannot be carried out for the longwave infrared wavelengths, which is also consistent with the simulation results. So, the enhancement effect of the surface plasmon coupling of microholes and microdisks is experimentally demonstrated. However, the measured spectra exhibited a clear deviation in the transmission peaks and bandwidths from those of the simulation. In order to investigate the reasons for the reduction of transmission, we carried out simulation experiments on three samples according to experimental structural parameters. As shown in Figure 9d,e, it can be seen that under these conditions, the transmission itself does decrease quite a bit. For example, in Figure 9d, compared with our designed hole–disk structure with optimal period of 2.6  $\mu\text{m}$ , due to the deviations in the radius between designed and measured values, the transmission peak is redshifted from designed 3.5  $\mu\text{m}$  to measured 4.0  $\mu\text{m}$ , and the peak transmission reduces from 99% to 45%. However, the metal disk has a great influence on the transmission of the compound hole–disk array. The enhanced effect of the metal disk on the transmission can be clearly seen in the simulation experiments. In those three structures with periods of 5.2, 5.6, and 5.8  $\mu\text{m}$ , the metal disk increases the transmission by 44%, 39%, and 38% respectively. With the corresponding period of these three structures increasing in turn, the corresponding transmission peak will gradually increase as expected. This phenomenon can be seen in both experimental and simulation results. For example, the transmission peak positions in the experimental results gradually increases from 5.1  $\mu\text{m}$  to 6  $\mu\text{m}$ , while the corresponding

simulation results gradually increase from 4  $\mu\text{m}$  to 4.4  $\mu\text{m}$ . We believe that the above comparisons can prove the feasibility of metal hole–disk coupled surface plasmon filter in practical detection. In addition, because of the lithography–coating–stripping method used in the preparation process, the metal surface is uneven, which creates a small, jagged residue. Oxidation of the metal aluminum on the surface may also lead to performance deviation to some extent, due to the change in the dielectric constant of the Al metal surface.

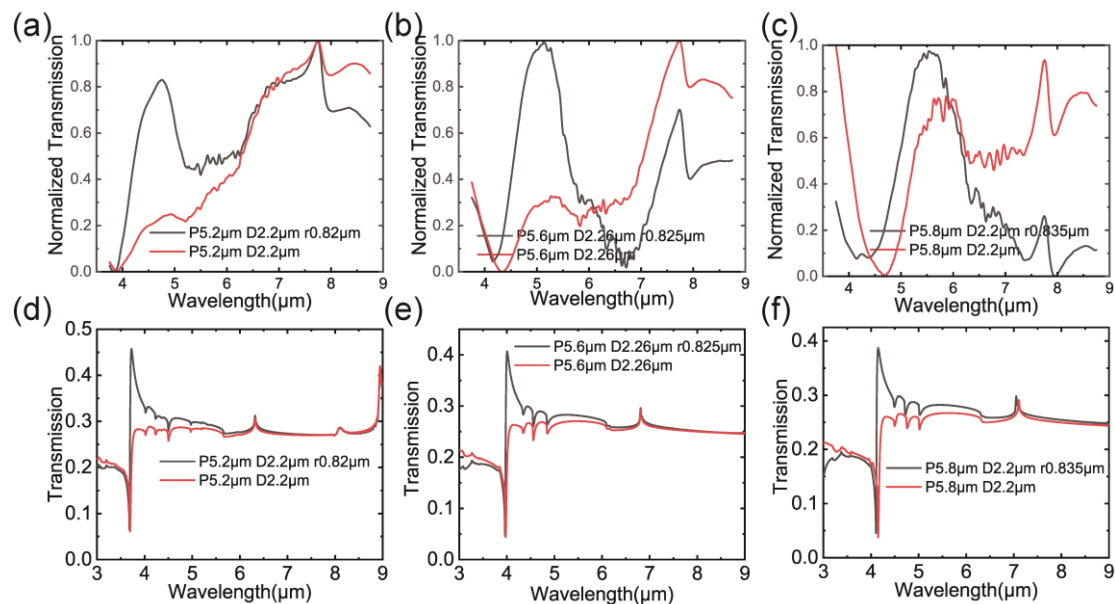


**Figure 9.** Measured normalized transmission spectra of three compound structures with different array periods compared with their counterparts of pure microhole structures. The three periods are  $P = 5.2 \mu\text{m}$  (a),  $P = 5.6 \mu\text{m}$  (b), and  $P = 5.8 \mu\text{m}$  (c). According to the experimental test results, the same structural parameters are used for simulation. The three periods are  $P = 5.2 \mu\text{m}$  (d),  $P = 5.6 \mu\text{m}$  (e), and  $P = 5.8 \mu\text{m}$  (f). Parameter  $r$  represent the radius of microdisk. The thickness of the cavity film is 80 nm and the height of the disk is 200 nm.

### 3. Conclusions

We proposed a silicon-based Al microhole and microdisk coupling array with an anomalous transmission filter. This hybrid structure of Al holes and disks can specifically transmit infrared light of a certain wavelength in the MLWIR at a very high transmission rate (99.1%) and a small FWHM. The device passes through the microdisk structure on the surface and the thin film of the microhole structure, which is attributed to the surface plasmon coupling between the hole and the disk array. The effect of the coupling enhancement at specific transmission peaks was proven through preliminary experiments. Under different structural parameters and background refractive indices, the near-perfect transmission peak exhibited high tunability and angle independence. We then described how to determine the central wavelength and optimal transmission of the device's transmitted infrared light. The exceptional transmission filter of the coupled array of microholes and microdisks, which can specifically transmit infrared light, will play a significant role in various optical fields.

**Author Contributions:** Conceptualization, L.X. and J.L.; methodology, L.X. and J.L.; validation, L.X.; resources, Y.G. and C.C.; writing—review and editing, L.X., Q.M., and C.C.; supervision, Q.M. and C.C.; project administration, Y.G. and C.C.; funding acquisition, J.L. All authors have read and agreed to the published version of the manuscript.

**Funding:** Funding was obtained from the National Key Research and Development of China (2020YFB2009302) and National Natural Science Foundation of China (61735018).

**Institutional Review Board Statement:** Not applicable.

**Informed Consent Statement:** Not applicable.

**Data Availability Statement:** Data is contained within the article.

**Acknowledgments:** We thank engineer Panpan Zheng from the Center of Optoelectronic Micro and Nano Fabrication and Characterizing Facility, Wuhan National Laboratory for Optoelectronics of Huazhong University of Science and Technology, for their support in device fabrication (stepper lithography).

**Conflicts of Interest:** The authors declare no conflicts of interest.

## References

1. Mohammadi, R.; Ochs, M.; Andrieu-Brunsen, A.; Vogel, N. Effect of Asymmetry on Plasmon Hybridization and Sensing Capacities of Hole-Disk Arrays. *J. Phys. Chem. C* **2020**, *124*, 2609–2618. [[CrossRef](#)]
2. Nishijima, Y.; Balčytis, A.; Seniutinas, G.; Juodkakis, S.; Arakawa, T.; Okazaki, S.; Petruškevičius, R. Plasmonic Hydrogen Sensor at Infrared Wavelengths. *Sens. Mater.* **2017**, *29*, 1269–1274.
3. Wang, B.; Yu, P.; Wang, W.; Zhang, X.; Kuo, H.-C.; Xu, H.; Wang, Z.M. High-Q Plasmonic Resonances: Fundamentals and Applications. *Adv. Opt. Mater.* **2021**, *9*, 2001520. [[CrossRef](#)]
4. Wang, X.; Zhang, J.; Zhu, J.; Yi, Z.; Yu, J. Refractive index sensing of double Fano resonance excited by nano-cube array coupled with multilayer all-dielectric film. *Chin. Phys. B* **2021**, *31*, 024210. [[CrossRef](#)]
5. Chen, Z.; Hu, R.; Cui, L.; Yu, L.; Wang, L.; Xiao, J. Plasmonic wavelength demultiplexers based on tunable Fano resonance in coupled-resonator systems. *Opt. Commun.* **2014**, *320*, 6–11. [[CrossRef](#)]
6. Zhou, Z.-K.; Su, X.-R.; Peng, X.-N.; Wang, Q.-Q.; Zhang, Q.; Shan, X.; Zhang, Z. 1 Tuning gold nanorod-nanoparticle hybrids into plasmonic Fano resonance for enhanced lightening and transmission. *Phys. Rev. Lett.* **2010**, *11*, 49–55.
7. Luk'yanchuk, B.; Zheludev, N.I.; Maier, S.A.; Halas, N.J.; Nordlander, P.; Giessen, H.; Chong, C.T. The Fano resonance in plasmonic nanostructures and metamaterials. *Nat. Mater.* **2010**, *9*, 707–715. [[CrossRef](#)]
8. Wang, X.; Wu, Y.; Wen, X.; Zhu, J.; Bai, X.; Qi, Y.; Yang, H. Surface plasmons and SERS application of Au nanodisk array and Au thin film composite structure. *Opt. Quantum Electron.* **2020**, *52*, 238. [[CrossRef](#)]
9. Wu, Y.; Wang, X.; Wen, X.; Zhu, J.; Bai, X.; Jia, T.; Yang, H.; Zhang, L.; Qi, Y. Surface-enhanced Raman scattering based on hybrid surface plasmon excited by Au nanodisk and Au film coupling structure. *Phys. Lett. A* **2020**, *384*, 126544. [[CrossRef](#)]
10. Barnes, W.L.; Dereux, A.; Ebbesen, T.W. Surface plasmon subwavelength optics. *Nature* **2003**, *424*, 824–830. [[CrossRef](#)]
11. Genet, C.; Ebbesen, T.W. Light in tiny holes. *Nature* **2007**, *445*, 39–46. [[CrossRef](#)] [[PubMed](#)]
12. Lezec, H.J.; Thio, T. Diffracted evanescent wave model for enhanced and suppressed optical transmission through subwavelength hole arrays. *Opt. Express* **2004**, *12*, 3629–3651. [[CrossRef](#)] [[PubMed](#)]
13. Li, Z.; Butun, S.; Aydin, K. Large-Area, Lithography-Free Super Absorbers and Color Filters at Visible Frequencies Using Ultrathin Metallic Films. *ACS Photonics* **2015**, *2*, 183–188. [[CrossRef](#)]
14. Biswas, R.; Paul, D. LSPR enhanced gasoline sensing with a U-bent optical fiber. *J. Phys. D Appl. Phys.* **2016**, *49*, 305104.
15. Lo, Y.-L.; Chuang, C.-H.; Lin, Z.-W. Ultrahigh sensitivity polarimetric strain sensor based upon D-shaped optical fiber and surface plasmon resonance technology. *Opt. Lett.* **2011**, *36*, 2489–2491. [[CrossRef](#)] [[PubMed](#)]
16. Papiya, D.; Vinod Kumar, S.; Massimo, O.; Guido, P. Reflectance-based low-cost disposable optical fiber surface plasmon resonance probe with enhanced biochemical sensitivity. *Opt. Eng.* **2016**, *55*, 046114.
17. Sage, A.T.; Besant, J.D.; Lam, B.; Sargent, E.H.; Kelley, S.O. Ultrasensitive Electrochemical Biomolecular Detection Using Nanostructured Microelectrodes. *Acc. Chem. Res.* **2014**, *47*, 2417–2425. [[CrossRef](#)]
18. Lord, H.; Kelley, S. Nanomaterials for ultrasensitive electrochemical nucleic acids biosensing. *J. Mater. Chem.* **2009**, *19*, 3127–3134. [[CrossRef](#)]
19. Guan, S.; Li, R.; Sun, X.; Xian, T.; Yang, H. Construction of novel ternary Au/LaFeO<sub>3</sub>/Cu<sub>2</sub>O composite photocatalysts for RhB degradation via photo-Fenton catalysis. *Mater. Technol.* **2021**, *36*, 603–615. [[CrossRef](#)]
20. Liu, C.; Wang, J.; Wang, F.; Su, W.; Yang, L.; Lv, J.; Fu, G.; Li, X.; Liu, Q.; Sun, T.; et al. Surface plasmon resonance (SPR) infrared sensor based on D-shape photonic crystal fibers with ITO coatings. *Opt. Commun.* **2020**, *464*, 125496. [[CrossRef](#)]
21. Liu, C.; Yang, L.; Liu, Q.; Wang, F.; Sun, Z.; Sun, T.; Mu, H.; Chu, P.K. Analysis of a Surface Plasmon Resonance Probe Based on Photonic Crystal Fibers for Low Refractive Index Detection. *Plasmonics* **2018**, *13*, 779–784. [[CrossRef](#)]
22. Sharma, A.K.; Gupta, B.D. Influence of temperature on the sensitivity and signal-to-noise ratio of a fiber-optic surface-plasmon resonance sensor. *Appl. Opt.* **2006**, *45*, 151–161. [[CrossRef](#)] [[PubMed](#)]
23. Pereira-Barros, M.A.; Nic Daeid, N.; Adegoke, O. Rapid and selective aptamer-based fluorescence detection of salivary lysozyme using plasmonic metal-enhanced fluorescence of ZnSSe alloyed quantum dots-gold nanoparticle nanohybrid. *J. Photochem. Photobiol. A Chem.* **2021**, *418*, 113384. [[CrossRef](#)]
24. Akceoglu, G.A.; Saylan, Y.; Inci, F. Point-of-Care Diagnostics: A Snapshot of Microfluidics in Point-of-Care Diagnostics: Multifaceted Integrity with Materials and Sensors (Adv. Mater. Technol. 7/2021). *Adv. Mater. Technol.* **2021**, *6*, 2170037. [[CrossRef](#)]

25. Prikulis, J.; Hanarp, P.; Olofsson, L.; Sutherland, D.; Käll, M. Optical Spectroscopy of Nanometric Holes in Thin Gold Films. *Nano Lett.* **2004**, *4*, 1003–1007.
26. Wang, Y.; Luong, H.; Zhang, Z.; Zhao, Y. Coupling between plasmonic nanohole array and nanorod array: The emerging of a new extraordinary optical transmission mode and epsilon-near-zero property. *J. Phys. D Appl. Phys.* **2020**, *53*, 275202. [[CrossRef](#)]
27. Du, Z.; Liu, H. Mid-infrared refractive index photonic crystal fiber sensor based on surface plasmon resonance for ultra-high sensitivity. *Laser Phys.* **2023**, *33*, 016201. [[CrossRef](#)]
28. Hosseini, E.; Mir, A.; Farmani, A. Black Phosphorous-Based Nanostructures for Refractive Index Sensing with High Figure of Merit in the Mid-infrared. *Plasmonics* **2022**, *17*, 639–646.
29. Kirlar, M.; Turkmen, M. Ultra narrowband perfect absorber for refractive index sensing applications in mid-infrared region. *J. Electromagn. Waves Appl.* **2023**, *37*, 803–813. [[CrossRef](#)]
30. Wu, C.; Khanikaev, A.B.; Adato, R.; Arju, N.; Yanik, A.A.; Altug, H.; Shvets, G. Fano-resonant asymmetric metamaterials for ultrasensitive spectroscopy and identification of molecular monolayers. *Nat. Mater.* **2012**, *11*, 69–75. [[CrossRef](#)]
31. Singh, A.; Lin, Y.-C.; Sheehan, C.; Dattelbaum, A.; Gupta, G.; Mohite, A. Millimeter-scale gate-tunable graphene nanoribbon devices as a platform for mid-infrared and bio sensing applications. *Appl. Mater. Today* **2016**, *4*, 40–44. [[CrossRef](#)]
32. Lertvachirapaiboon, C.; Baba, A.; Ekgasit, S.; Shinbo, K.; Kato, K.; Kaneko, F. Transmission surface plasmon resonance techniques and their potential biosensor applications. *Biosens. Bioelectron.* **2018**, *99*, 399–415. [[CrossRef](#)] [[PubMed](#)]
33. Yang, K.; Chen, Y.; Yan, S.; Yang, W. Nanostructured surface plasmon resonance sensors: Toward narrow linewidths. *Heliyon* **2023**, *9*, e16598. [[CrossRef](#)] [[PubMed](#)]
34. Hansen, P.M.; Bhatia, V.K.; Harrit, N.; Oddershede, L. Expanding the Optical Trapping Range of Gold Nanoparticles. *Nano Letters* **2005**, *5*, 1937–1942. [[CrossRef](#)]
35. Mrejen, M.; Israel, A.; Taha, H.; Palchan, M.; Lewis, A. Near-field characterization of extraordinary optical transmission in sub-wavelength aperture arrays. *Opt. Express* **2007**, *15*, 9129–9138. [[CrossRef](#)]
36. Silalahi, H.M.; Tsai, Y.-H.; Lee, K.-L.; Wei, P.-K.; Huang, C.-Y. Large shift of resonance wavelengths of silver nanoslit arrays using electrowetting-on-dielectric cells. *Opt. Lett.* **2021**, *46*, 705–708. [[CrossRef](#)]
37. Ung, B.; Sheng, Y. Optical surface waves over metallo-dielectric nanostructures: Sommerfeld integrals revisited. *Opt. Express* **2008**, *16*, 9073–9086. [[CrossRef](#)]
38. Du, B.; Yang, Y.; Zhang, Y.; Jia, P.; Ebendorff-Heidepriem, H.; Ruan, Y.; Yang, D. Enhancement of extraordinary optical transmission and sensing performance through coupling between metal nanohole and nanoparticle arrays. *J. Phys. D Appl. Phys.* **2019**, *52*, 275201. [[CrossRef](#)]
39. Wang, Z.; Hou, Y. High Optical Transmission in a Hybrid Plasmonic-Optical Structure with a Continuous Metal Film. *Plasmonics* **2018**, *13*, 1159–1163. [[CrossRef](#)]
40. Li, Z.; Gao, J.; Gao, J.; Yang, H.; Liu, H.; Wang, X.; Wang, T.; Wang, K.; Li, Q.; Liu, X.; et al. Linewidth reduction effect of a cavity-coupled dual-passband plasmonic filter. *Opt. Express* **2020**, *28*, 8753–8763.
41. Cheng, Y.; Zhang, H.; Mao, X.S.; Gong, R. Dual-band plasmonic perfect absorber based on all-metal nanostructure for refractive index sensing application. *Mater. Lett.* **2018**, *219*, 123–126. [[CrossRef](#)]
42. Verma, S.K.; Srivastava, S.K. Giant Extra-Ordinary Near Infrared Transmission from Seemingly Opaque Plasmonic Metasurface: Sensing Applications. *Plasmonics* **2022**, *17*, 653–663. [[CrossRef](#)] [[PubMed](#)]
43. Mobasser, S.; Poorgholam-Khanjari, S.; Bazgir, M.; Zarrabi, F.B. Highly Sensitive Reconfigurable Plasmonic Metasurface with Dual-Band Response for Optical Sensing and Switching in the Mid-Infrared Spectrum. *J. Electron. Mater.* **2021**, *50*, 120–128. [[CrossRef](#)]

**Disclaimer/Publisher’s Note:** The statements, opinions and data contained in all publications are solely those of the individual author(s) and contributor(s) and not of MDPI and/or the editor(s). MDPI and/or the editor(s) disclaim responsibility for any injury to people or property resulting from any ideas, methods, instructions or products referred to in the content.